RSC Advances

PAPER

View Article Online
View Journal | View Issue

Cite this: *RSC Adv.*, 2023, **13**, 28416

Efficient ternary WORM memory devices from quinoline-based D–A systems by varying the redox behavior of ferrocene†

Varghese Maria Angela,[a] Deivendran Harshini,[a] Predhanekar Mohamed Imran,[b] Nattamai. S. P. Bhuvanesh[c] and Samuthira Nagarajan *[a]

The design and synthesis of ferrocene-functionalized organic small molecules using quinoline cores are rendered to achieve a ternary write-once-read-many (WORM) memory device. Introducing an electron-withdrawing group into the ferrocene system changes the compounds' photophysical, electrochemical, and memory behavior. The compounds were synthesized with and without an acetylene bridge between the ferrocene unit and quinoline. The electrochemical studies proved the oxidation behavior with a slightly less intense reduction peak of the ferrocene unit, demonstrating that quinolines have more reducing properties than ferrocene with bandgaps ranging from 2.67–2.75 eV. The single crystal analysis of the compounds also revealed good interactive interactions, ensuring good molecular packing. This further leads to a ternary WORM memory with oxidation of the ferrocene units and charge transfer in the compounds. The devices exhibit on/off ratios of 10^4 and very low threshold voltages of −0.58/−1.02 V with stabilities of 10^3 s and 100 cycles of all the states through retention and endurance tests.

Received 20th August 2023
Accepted 7th September 2023

DOI: 10.1039/d3ra05685f

rsc.li/rsc-advances

Introduction

The demand and supply of information and its storage facility are comparatively low at the current information technology. The need for better storage devices in the current era of information technology is inevitable. The physical limitations and downscaling restraint of the conventional Si and Ge semiconductors led to progress in storage devices, focusing on the vast library of organic molecules.[1] The easily tunable organic small molecules in their donor–acceptor states can be highly advantageous. They could build in an intramolecular charge transfer along with the electron traps in compounds, producing a non-volatile nature in the memory devices.[2] Even when organic memory devices face many challenges regarding unclear switching behavior and ambiguous structure–property relationships, much research is going on in this area for enhancing memory performances.[3] Also, the advantage of using the resistance of the molecules to induce switching upon an applied voltage is highly beneficial for multilevel storage memories. The increase in conductive states of the devices could increase the storage density from 2^n to 3^n or 4^n, as per the number of conductive states.[4]

The incorporation of organometallic frameworks into the organic molecules is found to be an efficient strategy for the development of high-performance organic electronic devices.[5] This strategy is used in organic electronics such as biosensors,[6] organic light-emitting diodes,[7] organic batteries,[8] and organic memory devices.[9] Functionalized ferrocene is a common scaffold for organic electronic endeavors. The highly stable 18 e^- complex is a research hotspot because of its stable electrochemical properties, the possibility of three-dimensional networks, solution processability, and high thermal stability.[10] Ferrocenes are now considered potential materials in organic memory devices when incorporated with organic small molecules and polymers.[11] A redox-active non-volatile rewritable memory device that includes a ferrocene unit into a pyrene system was developed by Li *et al.* in 2019.[12] Ferrocene-containing poly(fluorenylethynylene)s were synthesized and characterized for organic memories using triphenylamine, thiophene, and carbazole as the donor units. The different substituents showed various memory behaviors, from WORM to flash memories.[13] Ferrocene derivatives embedded into polystyrene compounds exhibited ternary switching behavior with good on/off ratio.[14] Ferrocene-based fluorene derivatives with porphyrin and phenyl-based diethynyl ligands were designed and synthesized to show electrical bistability through a WORM memory device.[15]

Therefore, after carefully analyzing literature, in this work, we designed and synthesized six novel organic molecules by

[a]*Department of Chemistry, Organic Electronics Division, Central University of Tamil Nadu, Thiruvarur 610 005, India. E-mail: snagarajan@cutn.ac.in*

[b]*Department of Chemistry, Islamiah College, Vaniyambadi, 635 752, India*

[c]*Department of Chemistry, Texas A&M University, College Station, TX 77842, USA*

† Electronic supplementary information (ESI) available: Materials and methods and characterization data, thin film characterizations, cyclic voltammograms, computational analysis, memory device fabrication and studies. CCDC 2239172. For ESI and crystallographic data in CIF or other electronic format see DOI: https://doi.org/10.1039/d3ra05685f

incorporating functionalized ferrocene into the less explored quinoline unit. In the literature, we could find only ferrocene systems attached to electron-donating units, which usually act as an electron-accepting units due to the higher electron-donating power of the ferrocene unit. Integrating a ferrocene-electron withdrawing group has not been explored yet. A good electron-withdrawing group with electron traps could change the properties of the system and, thereby, the device's memory performance. Ferrocene and ferrocenium ions can both stay stable even in the absence of potential. Therefore, the incorporation of a ferrocene unit can bring about a change in the conductivity of the devices through the redox activity of the compounds.[16] These photophysical, electrochemical, morphological, electrical, and computational studies of the compounds were performed to understand the molecule's semiconducting properties. All of the compounds exhibited ternary WORM memory performance with good on/off ratios and very low threshold voltages. These compounds could therefore be considered better candidates in organic memory devices.

Result and discussion

Synthesis and characterization

The synthetic route for the targeted compounds **6a–c** and **7a–c** are given in Scheme 1, and the molecular structures of the

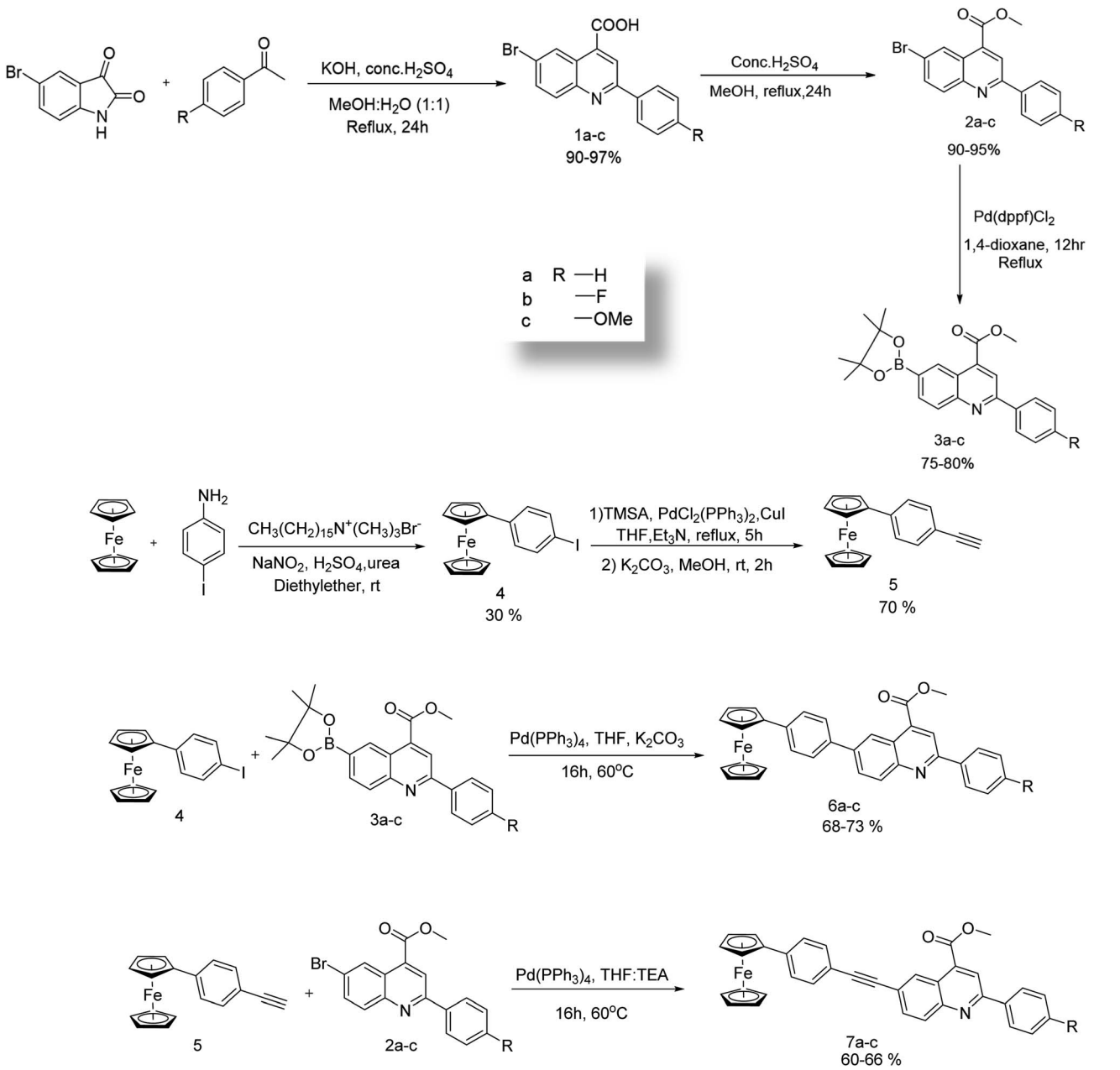

Scheme 1 Synthetic scheme for the synthesis of the targeted compounds **6a–c** and **7a–c**.

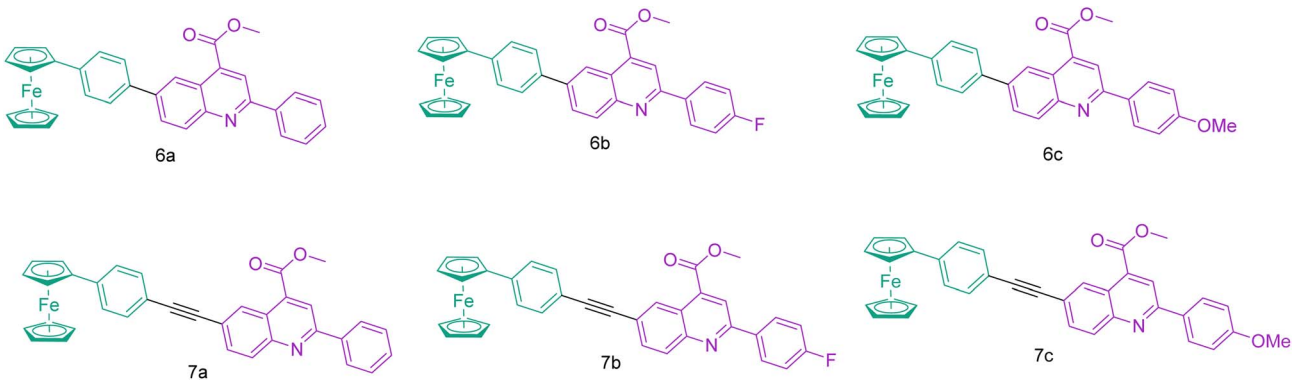

Fig. 1 Structure of the ferrocene-attached quinoline compounds.

targeted compounds are shown in Fig. 1. The synthetic precursors iodinated phenylferrocene and aryleneethynylene-ferrocene were synthesized through Scheme 1 and functionalized quinolines were synthesized through Pfitzinger reactions, followed by esterification and Miyura-borylation. The targeted compounds **6a–c** were synthesized through a Suzuki cross-coupling reaction between the corresponding quinoline boronic acid and compound **4**. Simultaneously, compound **5** reacted with the corresponding brominated quinolines under Sonagashira reaction conditions for 5–6 hours to get the compounds **7a–c**. All of these targeted compounds were synthesized in moderate to good yields, and are soluble in common organic solvents like DCM, THF, chloroform, and ethyl acetate. All of the compounds were thoroughly characterized using NMR, HRMS, and single-crystal XRD, and the results are provided in the ESI.† In the targeted compounds, the ferrocene unit acts as the donor molecule and the ester-flanked quinolines as the acceptor molecule, forming a D–A molecule with and without an acetylene bridge in between them. The ethylene bridges build rigidity and better conjugation in the compounds, whereas the different substitutions at the quinoline end help to understand the structure–property relationship of the compounds.

Photophysical studies

The optical properties of the synthesized compounds were initially investigated through UV-Vis and fluorescence spectroscopy in dichloromethane solution, as well as in its thin-film state. All of the donor–acceptor compounds (**6a–c** and **7a–c**) exhibited two bands (Fig. 2). The high energy absorption band with a λ ranging from 282–297 nm corresponds to the π–π^* transition from the aromatic conjugation of the compounds. The low energy band giving rise to a λ_{max} ranging from 367–387 nm arises from the intramolecular charge transfer (ICT) between the phenyl-substituted ferrocene donor molecule and the ester-flanked quinoline acceptor molecule. The red shift in the absorption maxima for the ICT in the compounds follows the order **7c** > **6c** > **7b** > **7a** > **6a** > **6b**. In general, compounds **7a–c** have a profound shift in the absorption maxima compared to compounds **6a–c**, which may be attributed to incorporation of an acetylene bond between the donor and acceptor molecules, increasing the conjugation and, thereby, the ICT of the compounds.[17] This redshift is highly visible in the thin film absorption spectra, in which even the intensity of the absorption maxima follows the same order as the redshift (Fig. S15†). The thin film absorption spectra thus prove to be beneficial for better ICT in the compounds arising from the better molecular

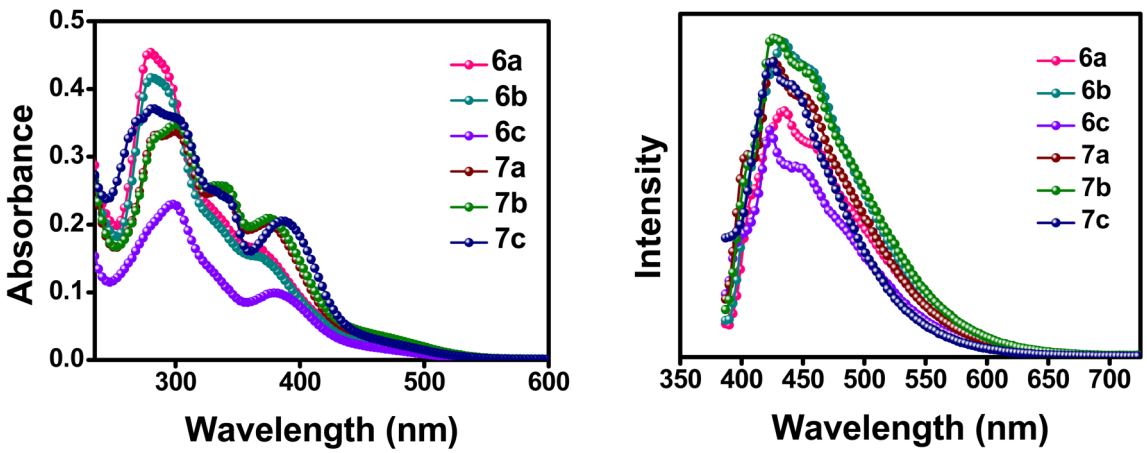

Fig. 2 Absorption (10^{-5} M) and emission (10^{-7} M) spectra of the compounds in DCM solution.

Table 1 Photophysical parameters of the compounds in DCM solution

Compounds	λ_{max} (abs) (nm)	λ_{max} (em) (nm)	Stokes shift (nm)	Absorption coefficient ($10^3 \times M^{-1}$ cm^{-1})
6a	368.8	435.8	66.9	16
6b	368.5	435.1	66.6	15
6c	381.7	425.7	43.9	10
7a	376.0	425.3	49.2	20
7b	377.3	428.3	50.9	20
7c	387.2	425.3	38.0	20

ordering of the compounds in their thin film state.[18] The emission spectra of the compounds were also taken, and all the compounds express a broad emission spectrum ranging from 390–600 nm. The intensity of the λ_{max} emission is also higher for compounds **7a–c** than that for compounds **6a–c**. This is convincingly true for their thin film emission spectrum also with even broader peaks ranging from 450–700 nm (Fig. S15†). The UV-Vis and emission spectra in the solution state and their calculated values are indicated in Fig. 2 and Table 1, respectively.

Electrochemical analysis

Incorporating the ferrocene unit into the quinoline-based small molecule increases the reduction behavior of the quinoline compounds. This enhanced reduction behavior has been studied using the cyclic voltammetry technique through a conventional three-electrode setup in dimethylformamide solvent (Fig. S16†). A reversible redox couple is seen at 0.54/0.46 V, which could be attributed to the oxidation and reduction potentials of the ferrocene center.[19] However, the reduction peak intensity in this redox couple is significantly reduced compared to the oxidation peak potential. The reduction peak due to the quinoline reduction, on the other hand, is prominent and has increased in intensity due to the addition of the ferrocene unit. This may be due to the efficient charge transfer in the compounds, which could lead to oxidation at one end of the donor molecule and reduction at the other end of the acceptor molecule. Thus, the electrons lost from the ferrocene unit are readily accepted by the quinoline unit, which enhances its peak intensities, furnishing an efficient D–A system.

The oxidation potential of the ferrocene unit is used to calculate the HOMO energy levels of the compounds using the equation $E_{HOMO} = -(4.8 + E_{ox} - E_{Fc/Fc^+})$. The LUMO energy levels have been calculated using the equation $E_{LUMO} = [E_{HOMO} - E_g]$, where the E_g is the optical bandgap of the compounds.[20] The HOMO and LUMO energy levels of the compounds range from −4.82 to −4.86 eV and −2.06 to −2.18 eV, respectively. The compounds' electrochemical bandgap ranges from 2.67–2.77 eV. Among these, compound **7c** with the methoxy substitution at the quinoline end has the lowest bandgap value. Despite the slight structural differences, compounds **7a–c** show a better bandgap value than **6a–c**, which may benefit the charge transfer processes expected for the memory behavior. The computational values for the HOMO, LUMO, and bandgap of the compounds are on par with the experimental ones, and are listed in Table 2.

Thin-film characteristics and single-crystal analysis

The microstructural packing of the compounds was studied through thin-film XRD to understand the crystalline nature of the compounds (Fig. 3). All of the compounds exhibit two intense peaks at 30.70° and 35.83°, corresponding to a *d*-spacing of 2.96 and 2.56 Å, respectively. These *d*-spacing values promise better molecular ordering with good interactive interactions. Also, the highly intense nature of the peaks shows the compounds crystallinity and long-range order. There are three less intense peaks for the compounds at an angle of 21.86°, 51.00°, and 60.66°, giving a *d*-spacing of 3.97, 1.79, and 1.54 Å, respectively.

The SEM images of the compounds were taken by coating a thin film of the compounds over an ITO-coated glass plate. All of the compounds exhibit full coverage even up to 10 μm, showing the tight packing of the compounds in the thin film (Fig. 4). All of the compounds display different morphologies owing to the different substitutions. Compounds **6a** and **7a** have petal-like morphologies, while **6b** and **6c** have terrain-like

Table 2 Electrochemical parameters of the compounds **6a–c** and **7a–c**

	Experimental				Computational		
Compound	E_{ox} (V)	E_{HOMO} (eV)	E_{LUMO} (eV)	E_g (eV)	E_{HOMO} (eV)	E_{LUMO} (eV)	E_g (eV)
6a	0.54	−4.84	−2.11	2.73	−5.17	−2.14	3.03
6b	0.53	−4.83	−2.06	2.77	−5.19	−2.20	2.99
6c	0.52	−4.82	−2.08	2.74	−5.13	−2.04	3.08
7a	0.54	−4.84	−2.09	2.75	−5.19	−2.25	2.93
7b	0.56	−4.86	−2.14	2.72	−5.21	−2.31	2.89
7c	0.55	−4.85	−2.18	2.67	−5.14	−2.17	2.96

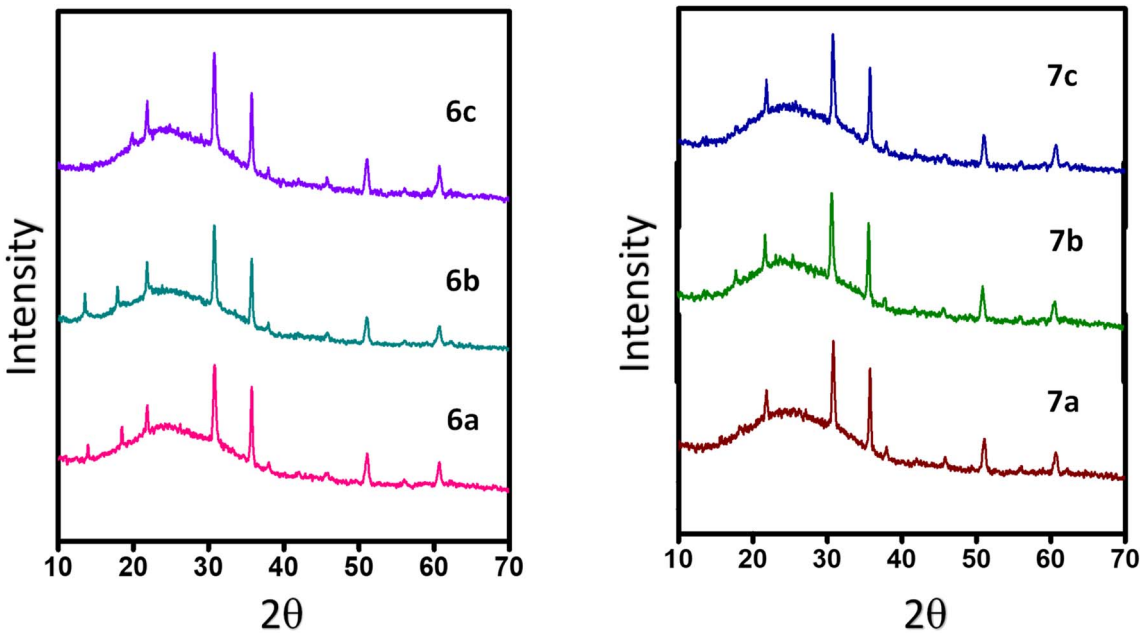

Fig. 3 Thin-film XRD analysis of the compounds **6a–c** and **7a–c**.

morphologies. Compound **7b** reveals a needle-like topography, whereas **7c** has a flower-like morphology. The SEM images of quinoline containing D–A molecules with similar morphologies have been reported in the literature.[21–23] All of the compounds exhibit good surface morphology without any deformities, favoring the charge transfer possibility of the compounds.

The compound **6a** was crystallized as a plate-shaped brown crystal by the slow evaporation of DCM: hexane in a 2 : 1 ratio. The single crystal analysis of this compound exhibited an orthorhombic crystal system in a *Pbcn* space group. The crystal packing was observed to have a herringbone-type arrangement, with the shortest interactive distance between two molecules being 3.019 Å (Fig. 5). The phenyl ring attached to the ferrocene unit was twisted from the plane to have a better π–π stacking between the compounds, enabling better molecular ordering in the compounds. The end-to-end packing of each molecule in the crystal and the stacking properties of the quinoline unit constitute better charge transport within the system.

Memory characteristics

The memory devices of the ferrocene-containing quinolines were fabricated by spin-coating the active layer over an ITO-

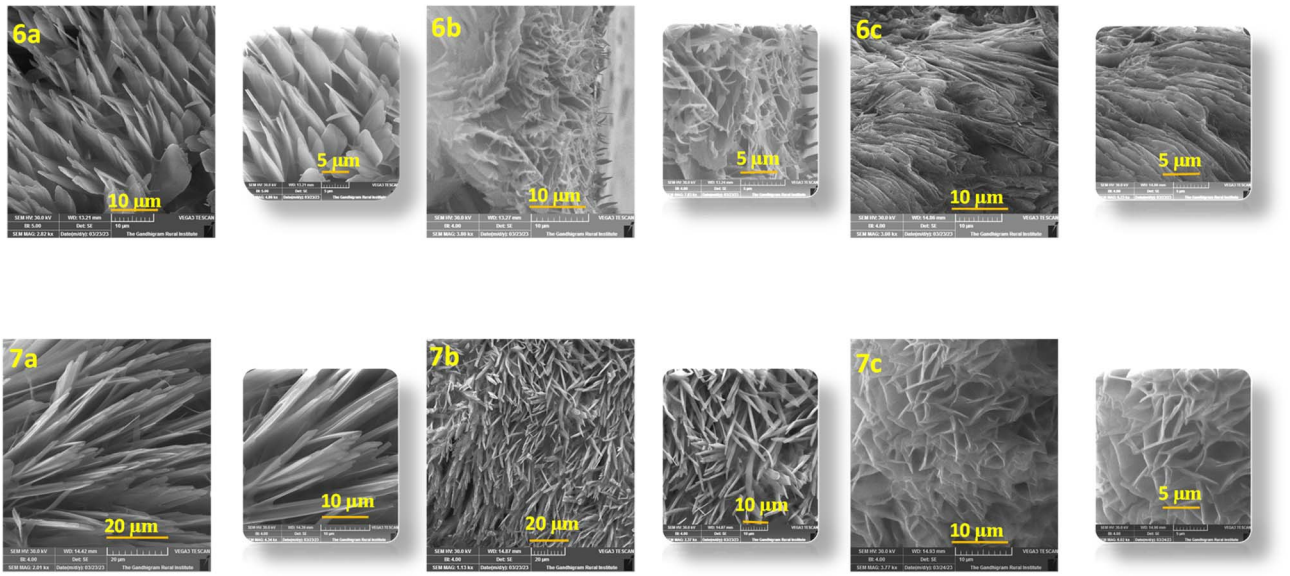

Fig. 4 SEM images of the compounds **6a–c** and **7a–c** at low and high magnification.

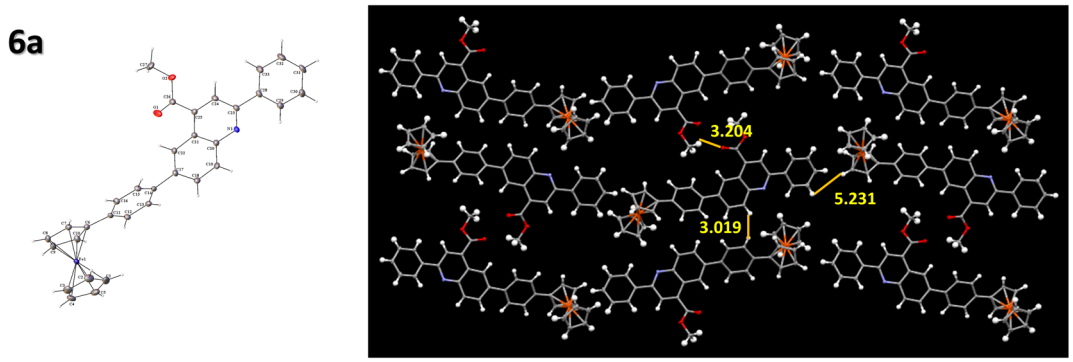

Fig. 5 Single crystal XRD of the compound **6a** with its packing pattern.

coated glass plate and sandwiching it between the Ag electrodes. Fig. 6 depicts the memory performance of the devices at a voltage sweep under ambient conditions. The device exhibits a typical non-volatile ternary WORM memory performance when the electric potential is applied between the top and the bottom electrodes.[24,25] Under an applied negative sweep from 0 to −3 V, the devices initially go from an OFF state to an intermediate ON1 state, which immediately switches to the ON2 state after the second threshold voltage. In the further positive and negative sweeps (0 to −3 and 0 to 3), this ON2 state is maintained, which is stable for more than 24 hours. This manifests the non-volatile nature of the memory devices even after the removal of power. Taking the redox active ferrocene unit in the targeted molecules, we expected a flash memory behavior, but ended up having a ternary WORM memory behavior. This may be due to the incorporation of an electron-withdrawing substituent into the redox system.

The OFF and ON states are stable for three orders of magnitude, allowing for distinguishing the three resistance states in the memory circuit (Fig. S21†). Simultaneously, the endurance cycle measurements ensure the device's endurance over 100 cycles under a constant stress voltage of −0.5 V (Fig. S20†). In other words, the almost invariable currents in the ON and OFF states after 4000 s or 100 cycles demonstrated the excellent stability of the prepared materials, indicating the potential practical application of ferrocene-containing quinolines in memory devices.[26] Moreover, the very low threshold voltage for both ON1 and ON2 states ensures low power consumption of these memory devices.[26]

Moreover, the very low threshold voltage for both ON1 and ON2 states ensures low power consumption of these memory devices. Among the compounds, **7a–c** shows better memory performance than **6a–c**. This is possibly due to the extended conjugation leading to better charge transfer in the compounds.

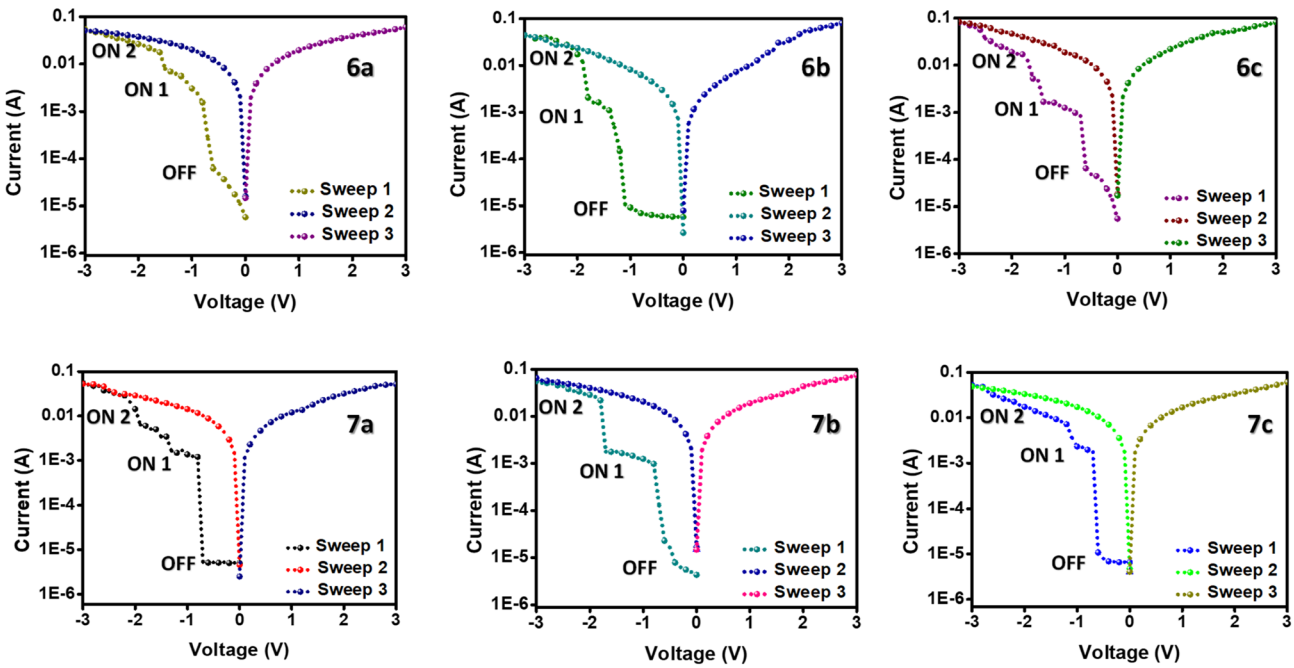

Fig. 6 *I–V* graphs of the memory devices **6a–c** and **7a–c**.

Table 3 Memory characteristics of the compounds 6a–c and 7a–c

Compound	On/off ratio[a]	Threshold voltage[a] (V)	
6a	10^3	−0.59	−1.41
6b	10^4	−1.02	−1.80
6c	10^3	−0.58	−1.37
7a	10^4	−0.65	−1.21
7b	10^4	−0.61	−1.61
7c	10^4	−0.58	−1.02

[a] calculated from the mean of 5 devices (20 cells).

The memory devices offer high on/off ratios ranging from 10^3 to 10^4 and very low threshold voltages of even −0.58 V, listed in Table 3. The on/off ratios of the compounds are higher than most of the small molecule-based, ferrocene-incorporated compounds in the literature.[12,27] The threshold voltages are even comparable with the ferrocene-containing polymer compounds, which assures lower power consumption of the memory devices.[13,14]

The operational model in the ternary WORM memory devices was simulated by plotting a log *I*–log *V* graph, as shown in Fig. 7. Initially, the slope of the graph is fitted to 0.99 in the OFF state of the devices, indicating an ohmic conductance (*I*–*V*) at the low resistance state. But as the voltage bias increases beyond the threshold voltage, the slope also changes to 3.11 and 2.58, suggesting a change in the conduction from ohmic to Childs' Square law (I–V^2).[28] The intermediate conduction state also follows the Childs' Square law and is dominated by the trap-filled space charge limited current (SCLC) conduction mechanism.[29] Upon further increase of the voltage, the slope falls back to 1.00, obtaining the ohmic conduction again. This trap-filled SCLC conduction model type is suitable for all memory devices **6a–c** and **7a–c**. As the voltage sweep exceeds the threshold voltage, the traps in the molecules are filled, and the conductivity increases to the ON2 state. Therefore, the trap-filled SCLC model induces the electrical switching characteristics in these memory devices.

Resistive switching mechanism

For a careful understanding of the resistive switching mechanism of the memory devices, the HOMO–LUMO energy levels of the compounds were analyzed through DFT methods. It was found that the compounds' HOMO levels reside on the electron-donating ferrocene unit, whereas the LUMO levels have more electron density towards the electron-withdrawing quinoline ends (Fig. 8). This constitutes an efficient charge transfer possibility from the HOMO to LUMO levels under an applied voltage. But, further charge transfer into the LUMO+1 and LUMO+2 levels is not seen as these levels' electron densities reside over the whole molecule. Therefore, subsequent charge transfers into the higher molecular energy levels are restricted. It is also found from the HOMO–LUMO energy values that the hole transfer from the ITO to the HOMO of the compounds is much more feasible than the electron transfer from the Ag electrode to the LUMO level. This allows holes to be major carriers in these memory devices. The compounds' electrostatic potentials (ESP images) were also scrutinized, which clearly showed ferrocene to be an electron-donating moiety, while the quinolines are the electron-withdrawing moiety (Fig. 9). The red regions in the compounds mainly situated at the quinoline ends can act as traps and hold in the charges transported within the device. These traps are the reason for the non-volatile nature of these memory devices proving essential for the ternary WORM memory behavior. This type of ternary WORM memory behavior is not seen in compounds with ferrocene containing small

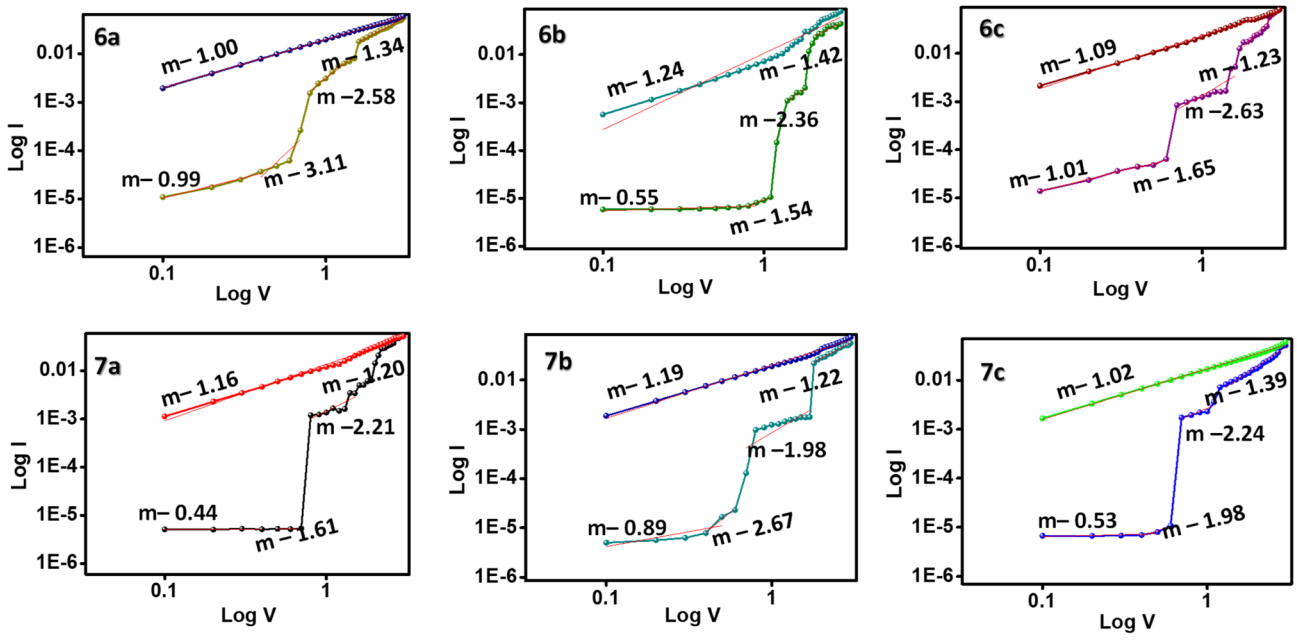

Fig. 7 log *I*–log *V* graphs of the memory devices for investigating the operational model.

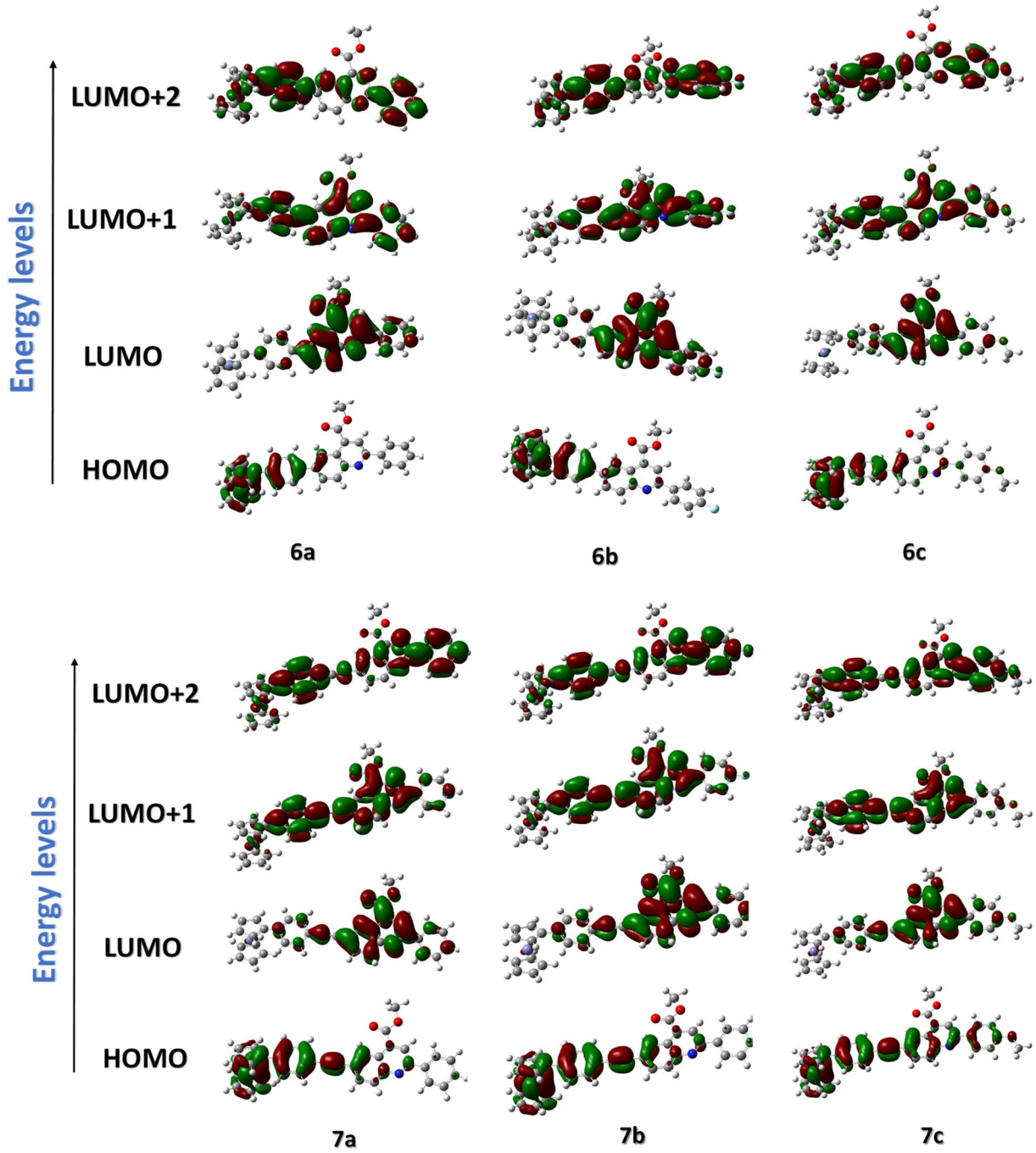

Fig. 8 Electron density on HOMO, LUMO, LUMO+1, and LUMO+2 levels of the compounds **6a–c** and **7a–c**.

molecules or polymers due to the highly robust nature of the ferrocene unit leading to the flash memory characteristics.

Therefore, by carefully analyzing the *I–V* characteristics, the redox behavior through CV, and the HOMO–LUMO and ESP diagrams through DFT methods, we could conclude that substituting the redox-active system with the electron-donating or withdrawing molecules plays a crucial role in deciding the memory behavior of the system. The electrochemical properties of the compounds are tuned by attaching the ferrocene system to an electron-withdrawing substituent. Substituting the ferrocene unit to electron-donating substituents like triarylamine or thiophene tends to result in the compounds being donor–acceptor units. Here, the electron-donating substituents act as the accepting unit due to the greater donating power of the ferrocene system.[12,13,27] Therefore, attaching the ferrocene unit with an electron-accepting substituent changes the redox behavior and, thereby, the device characteristics simultaneously.

The higher on/off ratios of the compounds **7a–c** compared to **6a–c** are also seen from the electrochemical oxidation occurring

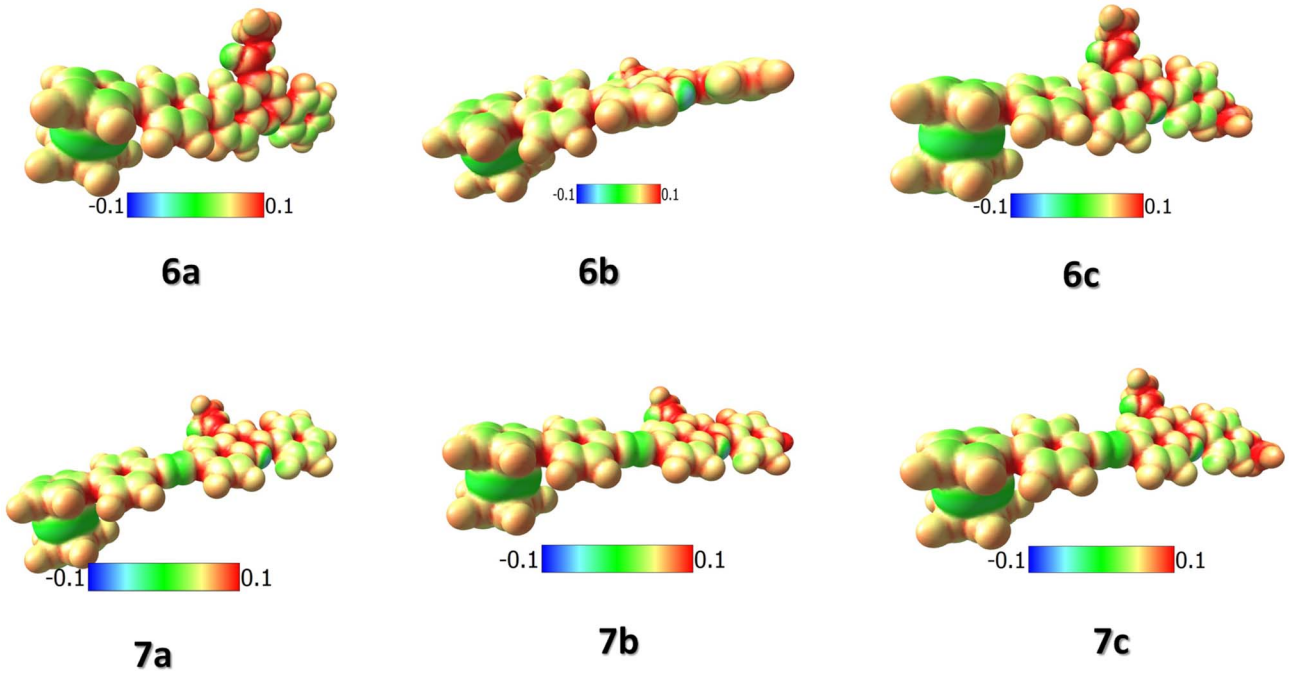

Fig. 9 MESP diagrams of the compounds **6a–c** and **7a–c**.

in the compounds. The compounds **7a–c** have a better oxidation current intensity of the ferrocene unit, indicating the faster electron transfer ability of these compounds. Also, the ethynyl spacer between the compounds could increase the π-conjugation and thereby increase the charge transfer in the compounds. The low threshold voltages promise the oxidation of the ferrocene unit in the first threshold, followed by the charge transfer in the compounds in the second threshold voltage.

Thus, the mechanism involves the following steps: In the first sweep from 0 to −3, after attaining the threshold voltage, the ferrocene unit loses one electron to become the ferrocenium ion. This leads to the first switching from OFF to ON1 state. After this oxidation, the lost electron is readily accepted by the quinoline end due to the higher electron-withdrawing property of the quinoline molecule. Then, a charge transfer happens from the ferrocene to the quinoline units, guiding the second switch from the ON1 to ON2 states. Due to the electron traps in the quinoline units, the charges trapped in them are not easily released and result in the devices' non-volatile ternary WORM memory behavior.

Conclusions

In conclusion, we have designed and synthesized six novel organic molecules with quinoline as the core molecule attached to the redox-active ferrocene unit. All of the compounds were thoroughly characterized using ^{1}H NMR, ^{13}C NMR, HRMS, and single-crystal XRD techniques. The solution and thin-film photophysical analyses exhibited an intramolecular charge transfer within the system, while the electrochemical analysis exhibited a less intense reduction peak of the ferrocene unit with a band gap ranging from 2.67–2.77 eV. The thin-film morphological studies (SEM and XRD) exhibited a highly crystalline nature, along with the total surface coverage of the compounds in the thin film. The memory device fabrication and characterization of the compounds yielded the devices' excellent ternary WORM memory behavior. The high on/off ratios of 10^4 and very low threshold voltages of 0.58/1.02 V ensure the possibility of new pathways for downscaling and multilevel storage devices through organic molecules. The devices are stable for over 4×10^3 s and 100 cycles, providing experimental proof for non-volatile small molecule-based organic memory devices incorporating an organometallic framework.

Author contributions

Varghese M. Angela: synthesis, methodology, data curation, data interpretation, design, and writing – original draft. Deivendran Harshini: methodology, review, and editing. Pradhanekar M. Imran: computational analysis. Nattamai. S. P. Bhuvanesh: single-crystal XRD analysis, Samuthira Nagarajan: project administration, supervision, review, and editing.

Conflicts of interest

There are no conflicts to declare.

Acknowledgements

The authors acknowledge the Central University of Tamil Nadu for its research facilities.

References

1 Y. Li, Q. Qian, X. Zhu, Y. Li, M. Zhang, J. Li, C. Ma, H. Li, J. Lu and Q. Zhang, *InfoMat*, 2020, **2**, 995–1033.
2 L. Yuan, S. Liu, W. Chen, F. Fan and G. Liu, *Adv. Electron. Mater.*, 2021, **7**, 1–35.
3 W. Banerjee, *Electron*, 2020, **9**, 1–24.
4 S. Gao, X. Yi, J. Shang, G. Liu and R. W. Li, *Chem. Soc. Rev.*, 2019, **48**, 1531–1565.
5 F. Bigdeli, C. T. Lollar, A. Morsali and H. C. Zhou, *Angew. Chem., Int. Ed.*, 2020, **59**, 4652–4669.
6 Y. Wu, X. Chen, X. Wang, M. Yang, F. Xu, C. Hou and D. Huo, *Sens. Actuators, B*, 2021, **329**, 129249.
7 C. L. Ho, H. Li and W. Y. Wong, *J. Organomet. Chem.*, 2014, **751**, 261–285.
8 C. Li, Q. Zhang, J. Sun, T. Li, S. Songfeng, Z. Zhu, B. He, Z. Zhou, Q. Li and Y. Yao, *ACS Energy Lett.*, 2018, **3**, 2761–2768.
9 H. Lian, X. Cheng, H. Hao, J. Han, M. T. Lau, Z. Li, Z. Zhou, Q. Dong and W. Y. Wong, *Chem. Soc. Rev.*, 2022, **51**, 1926–1982.
10 D. Astruc, *Eur. J. Inorg. Chem.*, 2017, **2017**, 6–29.
11 J. Y. Shao, B. Bin Cui, J. H. Tang and Y. W. Zhong, *Coord. Chem. Rev.*, 2019, **393**, 21–36.
12 Y. Li, X. Zhu, Y. Li, M. Zhang, C. Ma, H. Li, J. Lu and Q. Zhang, *ACS Appl. Mater. Interfaces*, 2019, **11**, 40332–40338.
13 J. Xiang, T. K. Wang, Q. Zhao, W. Huang, C. L. Ho and W. Y. Wong, *J. Mater. Chem. C*, 2016, **4**, 921–928.
14 Y. Z. Liu, Y. Liu, B. J. Chen, H. L. Yang, X. L. Lin, H. H. Li and Z. R. Chen, *Mater. Today Commun.*, 2022, **33**, 105026.
15 X. Cheng, A. Md, H. Lian, Z. Zhong, H. Guo, Q. Dong and V. A. L. Roy, *J. Organomet. Chem.*, 2019, **892**, 34–40.
16 J. Xiang, X. Li, Y. Ma, Q. Zhao, C. L. Ho and W. Y. Wong, *J. Mater. Chem. C*, 2018, **6**, 11348–11355.
17 B. S. Arslan, S. N. Ülüş, M. Gezgin, B. Arkan, E. Güzel, D. Avcı, M. Nebioğlu and İ. Şişman, *Opt. Mater.*, 2020, **106**, 109974.
18 A. Upadhyay and S. Karpagam, *Polym. Bull.*, 2016, **73**, 2741–2760.
19 G. Roy, R. Gupta, S. Ranjan Sahoo, S. Saha, D. Asthana and P. Chandra Mondal, *Coord. Chem. Rev.*, 2022, **473**, 214816.
20 A. Anjali, R. Dheepika, P. M. Imran, N. S. P. Bhuvanesh and S. Nagarajan, *ACS Appl. Electron. Mater.*, 2020, **2**, 2651–2661.
21 Z. Razmara, M. S. M. Abdelbaky and S. García-Granda, *J. Mol. Struct.*, 2019, **1197**, 217–226.
22 V. Kumar, M. Gohain, J. H. Van Tonder, S. Ponra, B. C. B. Bezuindenhoudt, O. M. Ntwaeaborwa and H. C. Swart, *Opt. Mater.*, 2015, **50**, 275–281.
23 C. Gogoi and S. Biswas, *Dalton Trans.*, 2018, **47**, 14696–14705.
24 Z. Liu, J. He, H. Li, Q. Xu, N. Li, D. Chen, L. Wang, X. Chen, K. Zhang and J. Lu, *Adv. Electron. Mater.*, 2016, **2**, 1–8.
25 X. Hou, X. Xiao, Q. H. Zhou, X. F. Cheng, J. H. He, Q. F. Xu, H. Li, N. J. Li, D. Y. Chen and J. M. Lu, *Chem. Sci.*, 2017, **8**, 2344–2351.
26 R. Hao, N. Jia, G. Tian, S. Qi, L. Shi, X. Wang and D. Wu, *Mater. Des.*, 2018, **139**, 298–303.
27 M. Zhang, C. Ma, D. Du, J. Xiang, S. Yao, E. Hu, S. Liu, Y. Tong, W. Y. Wong and Q. Zhao, *Adv. Electron. Mater.*, 2020, **6**, 1–7.
28 Z. He, X. Chen, H. Yu, Y. Du, M. Gao, S. Wang and C. Wang, *Chem. Eng. J.*, 2023, **457**, 141365.
29 G. Tian, S. Qi, F. Chen, L. Shi, W. Hu and D. Wu, *Appl. Phys. Lett.*, 2011, **98**, 1–4.